Noname manuscript No.
(will be inserted by the editor)

Geostatistical modelling of cyclic and rhythmic facies architectures

Thomas Le Blévec · Olivier Dubrule · Cédric M. John · Gary J. Hampson

Received: 27/10/2017 / Accepted:

Abstract A pluri-Gaussian method is developed for facies variables in three dimensions to model vertical cyclicity, related to facies ordering, and rhythmicity. Cyclicity is generally characterized by shallowing or deepening-upward sequences and rhythmicity by a low range of variability in cycle thicknesses. Both of these aspects are commonly observed in shallow-marine carbonate successions, especially in the vertical direction. A grid-free spectral simulation approach is developed, with a separable covariance allowing a dampened hole-effect to capture rhythmicity in the vertical direction and a different covariance in the lateral plan, along strata as in space-time models. In addition, facies ordering is created by using a spatial shift between two latent Gaussian functions in the pluri-Gaussian approach. Rapid conditioning to data is performed via Gibbs sampling and kriging using the screening properties of separable covariances. The resulting facies transiograms can show complex patterns of cyclicity and rhythmicity. Finally, a three dimensional case study of shallow-marine carbonate deposits at outcrop shows the applicability of the modeling method.

Keywords Pluri-Gaussian · asymmetric facies ordering · hole-effect · separable · transiogram · carbonate

T. Le Blevec
Earth Science and Engineering, Imperial College, London, United Kingdom
E-mail: t.le-blevec15@imperial.ac.uk
+447 466 892 985
Royal School of Mines, Prince Consort Road, London SW7 2BP, United Kingdom

O. Dubrule
Earth Science and Engineering, Imperial College and Total, London, United Kingdom

C. John
Earth Science and Engineering, Imperial College, London, United Kingdom

G. Hampson
Earth Science and Engineering, Imperial College, London, United Kingdom

1 Introduction

Spatial distributions of facies in sedimentary rocks are commonly characterized by cyclicity and rhythmicity in the vertical direction, and a variety of lateral patterns along stratigraphy. The resulting facies architectures control heterogeneity in hydrocarbon reservoirs and groundwater aquifers. It is therefore important to represent them in three-dimensional geostatistical earth models that are used as input to flow simulations and reserves quantification (Pyrcz and Deutsch, 2014).

Cyclicity is defined by a characteristic facies ordering in vertical successions (Wilkinson et al, 1997; Burgess, 2016). The characterization of cyclicity needs to be addressed statistically (Wilkinson et al, 1997) in order to apprehend the variability of the resulting facies patterns and to reproduce them in earth models. Facies cycles show preferential transitions between successive facies, such that one facies is preferentially observed on top of another facies. This is called asymmetry (Carle and Fogg, 1996), because the transitions between facies differ between the upward and downward directions. For example, shallow-marine carbonate rocks at outcrops (Strasser, 1988; Goldhammer et al, 1990) and in subsurface reservoirs (Lindsay et al, 2006) are typically characterized by facies cycles that record upward shallowing (regression) and that consist of subtidal facies overlain by intertidal facies overlain by supratidal facies. The facies succession that records upward deepening is commonly incomplete or absent, due to non-deposition or erosion, such that supratidal facies are directly overlain by subtidal facies, which mark the base of a new cycle. Such sequences are illustrated in Figs. 1c and 1d.

Classical geostatistical methods such as Sequential Indicator Simulation (Alabert, 1989) or object-based methods (Deutsch and Tran, 2002) are not able to reproduce this facies ordering because the facies are modelled independently from each other and so the transitions between facies cannot be constrained. However, the representation of asymmetry and facies ordering is possible with Markov Chains (Carle and Fogg, 1996; Parks et al, 2000; Purkis et al, 2012; Li, 2007) or renewal processes (Matheron, 1968), which are based on probabilities of transition between facies computed on the data and are directly inferred as parameters of the method.

Rhythmicity is another important aspect observed in vertical facies successions. It occurs where the thickness variability of vertically stacked facies cycles is low, a feature which has commonly been used to interpret periodic processes of deposition (e.g. via analysis of Fischer plots, Read and Goldhammer (1988)). Note that periodic processes (i.e. repetitive processes when looking at a time series) can either result in rhythmic sequences (when sedimentation rates are similar from cycle to cycle) or non rhythmic sequences (if sedimentation rates change between cycles). Because the space domain is considered here, we use the term rhythmicity rather than periodicity. Rhythmic stacking of facies cycles has been observed in many shallow-marine carbonate successions (Goldhammer et al, 1993; Egenhoff et al, 1999; Lindsay et al, 2006).

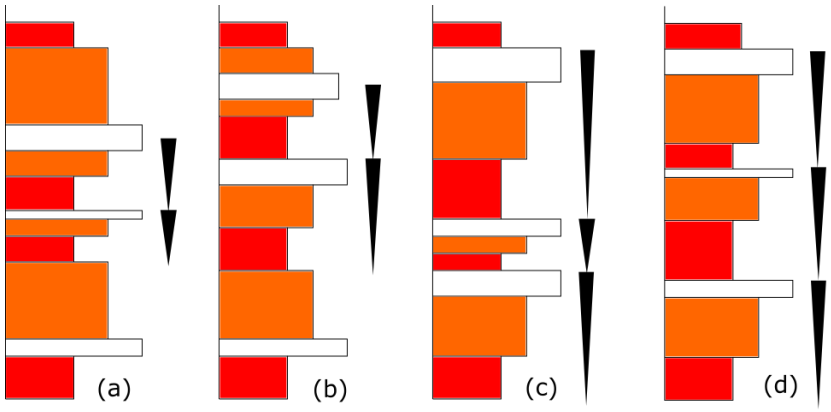

Fig. 1 Synthetic examples of facies sequences: (a) non cyclic non rhythmic, (b) non cyclic but red facies presents rhythmicity, (c) cyclic non rhythmic (d) cyclic rhythmic

This aspect is also shown in Figs. 1b (red facies) and 1d in which thicknesses between different beds of the same facies are constant.

Rhythmicity can be quantified by geostatistical tools, such as the variogram and the transiogram which show oscillations or dampened oscillations called hole effects (Pyrcz and Deutsch, 2014). By looking at the probability density function (pdf) of facies thicknesses, Ma and Jones (2001) show that as the coefficient of variation of this pdf decreases, the hole effect becomes more pronounced. This observation is in agreement with the above remark that rhythmicity is associated with low thickness variability of vertically stacked facies cycles. This also explains why Markov chains cannot create hole-effect transiogram models (Dubrule, 2017), as the corresponding thickness pdf is exponential (coefficient of variation equal to one). On the other hand, renewal processes may be able to create dampened hole-effect transiograms, because they offer the possibility to choose a thickness pdf with a lower coefficient of variation (Matheron, 1968). However, the transiograms derived from renewal processes are not always known analytically, and are thus difficult to adapt well to the observed rhythmicity.

Truncated or (pluri-) Gaussian methods have also been successfully used to create facies models (Armstrong et al, 2011), and they have been applied to shallow-marine carbonate reservoirs and outcrop analogues (Amour et al, 2012; Doligez et al, 2011; Le Blévec et al, 2017). The contacts between facies are defined by the truncation rule applied to a random Gaussian function, which provides control on facies juxtapositions. However, in its traditional form the method does not incorporate cyclicity and rhythmicity. Le Blévec et al (2017) have extended the Pluri-Gaussian method to the modelling of facies asymmetry in vertical successions, thus creating cyclicity. They produce asymmetric transition probabilities between facies by introducing a shift in the correlation of two random Gaussian functions as suggested by Armstrong et al (2011). This is similar to the approaches of Langlais et al (2008); Renard and

Beucher (2012), but with more flexibility in the resulting facies transiograms. Pluri-Gaussian simulations also enable the use of hole effect models (Beucher and Renard, 2016) and may lead to hole effect facies transiograms that can generate rhythmicity.

Although cyclicity and rhythmicity are common features of vertical facies successions, they may have a variable expression laterally, depending on the formative depositional processes and controls. Laterally extensive facies in shallow-marine carbonate strata are generally attributed to external (allogenic) controls that operated over an entire carbonate platform or shelf, such as relative sea-level variations (Goldhammer et al, 1990). Facies of limited lateral extent may be attributed to the nucleation, vertical build-up and lateral shifting of tidal flat islands across a carbonate platform or shelf (Pratt and James, 1986). This mechanism is internal to the dynamics of the carbonate platform depositional system (autogenic) and may generate both vertical and horizontal asymmetry in the stacking of facies if the tidal-flat-island deposits obey Walthers Law (Burgess et al, 2001; Le Blévec et al, 2016). Cyclic and rhythmic facies successions can also be overprinted by diagenetic facies after deposition; for example, hydrothermal dolomite bodies associated with faults and igneous intrusions are observed to cut across shallow-marine carbonate platform deposits characterized by rhythmic facies cycles (Jacquemyn et al, 2015).

In order to model two-dimensional areas and three-dimensional volumes that exhibit cyclic and rhythmic vertical facies successions but different lateral facies patterns, it is necessary to use different vertical and lateral covariance models. This is possible via the use of separable anisotropic models (Chiles and Delfiner, 2012), although such models have rarely been used for facies modelling (Matheron et al, 1988).

The aim of this paper is to develop a general method based on Pluri-Gaussian simulations to model facies cyclicity and rhythmicity in the vertical direction, and a range of appropriate lateral facies patterns using space-time (lateral-vertical) separable covariance models. After presenting the main definitions, the three key aspects of the modelling method and their impact on the transiograms are presented: cyclicity, rhythmicity, separability. A method for simulating the resulting complex facies architectures is then presented, firstly for unconditional simulations and then for simulations conditioned to data. Finally, the method is applied to a case study from the Triassic Latemar carbonate platform (northern Italy), which has been widely interpreted to show cyclicity and rhythmicity.

2 Definitions

2.1 Geostatistical quantification with transiograms

The random function representing a facies is the indicator function $I(x)$. If the facies i is present at a spatial location x, $I_i(x) = 1$ and if not, $I_i(x) = 0$. In

the stationary case, the probability of having a facies at a location x is equal to the first statistical moment or proportion

$$p_i = E[I_i(x)] = Pr\{I_i(x) = 1\}. \tag{1}$$

The presence of a facies also depends on the surrounding facies, quantified by the covariance function $C(h)$. With the stationary assumption, it is assumed that the covariance depends only on the vector separating two locations (Chiles and Delfiner, 2012). This paper uses the non-centered indicator covariance

$$C_{ij}(h) = Pr\{I_i(x) = 1, I_j(x+h) = 1\}, \tag{2}$$

from which can be derived the transiogram $t_{ij}(h)$, which is the probability to transition from facies i to facies j in a certain direction h

$$t_{ij}(h) = Pr\{I_j(x+h) = 1 | I_i(x) = 1\} = \frac{C_{ij}(h)}{p_i}. \tag{3}$$

This transiogram can be asymmetrical, which means that it is different in opposite direction

$$t_{ij}(h) \neq t_{ij}(-h), \tag{4}$$

and can thus quantify asymmetrical facies successions (Carle and Fogg, 1996; Le Blévec et al, 2017). The transiograms between different facies are usually gathered in a transiogram matrix that the simulation method aims to reproduce. For instance, a transition matrix between three facies $1, 2, 3$ is

$$t(h) = \begin{bmatrix} t_{11}(h) & t_{12}(h) & t_{13}(h) \\ t_{21}(h) & t_{22}(h) & t_{23}(h) \\ t_{31}(h) & t_{32}(h) & t_{33}(h) \end{bmatrix}. \tag{5}$$

The terms on the diagonal are the auto-transiograms and those off-diagonal are the cross-transiograms. The tangent at the origin of the auto-transiograms T_{ii} is related to the mean length of the facies i along this direction (Carle and Fogg, 1996). The tangent at the origin of the cross-transiogram is called the transition rate

$$T_{ij} = t'_{ij}(0). \tag{6}$$

Transition rates are interesting when studying asymmetry because they are related to juxtaposition between different facies. According to Carle and Fogg (1996), if a facies j tends to overlie a facies i, rather than being overlaid by it then

$$T_{ij} > \frac{p_j}{p_i} T_{ji}. \tag{7}$$

Transition rates are also related to embedded transition probabilities r_{ij} (given the presence of a facies i, the probability that it is overlaid by j)

$$r_{ij} = \frac{-T_{ij}}{T_{ii}}, \tag{8}$$

which can also be gathered in a transition matrix

$$R = \begin{bmatrix} 0 & r_{12} & r_{13} \\ r_{21} & 0 & r_{23} \\ r_{31} & r_{32} & 0 \end{bmatrix}. \tag{9}$$

The diagonal equals zero because embedded Markov chains only record the transitions between different facies. In the next section, it is shown how a geostatistical simulation method, the Truncated Gaussian Simulation, relates to these quantities.

2.2 Truncated Gaussian simulations

The truncated Gaussian (TGS) and Pluri-Gaussian (PGS) simulation (Armstrong et al, 2011) consist of simulating one or several continuous standardized bi-Gaussian fields that are then truncated into a facies field. A bi-Gaussian field $Z(x)$ is a random function such that any pair $(Z(x), Z(x+h))$ is a bi-Gaussian random vector, with $Z(x)$ and $Z(x+h)$ correlated to each other according to the non-centered covariance function

$$\rho(h) = E[Z(x)\ Z(x+h)]. \tag{10}$$

The truncation rule determines which facies is present at location x from the value of the random variables $Z(x)$. For instance, the truncation rule for two facies i and j with only one Gaussian function (TGS) controls the indicator functions

$$I_i(x) = 1 \quad I_j(x) = 0 \text{ if } \ Z(x) < q, \tag{11a}$$

$$I_i(x) = 0 \quad I_j(x) = 1 \text{ if } \ Z(x) \geq q, \tag{11b}$$

where q is the threshold of the truncation rule. It is possible to mathematically relate every moment of the facies field to those of the Gaussian function. According to Eq. (11a) the proportion of facies i (first order moment) is

$$p_i = \int_{-\infty}^{q} g(x)\ dx, \tag{12}$$

with $g(x)$ the standardized Gaussian pdf. The transition probability (second order moment) between facies i and j is

$$t_{ij}(h) = \frac{1}{p_i} \int_{-\infty}^{q} \int_{-\infty}^{q} g_{\rho(h)}(x, y)\ dx\ dy, \tag{13}$$

where $g_{\rho(h)}$ a standardized bi-Gaussian probability density with correlation matrix defined by the covariance $\rho(h)$. For $q = 0$ the two facies have same proportion $1/2$ and the analytical solution of this bi-Gaussian integral (Lantuéjoul, 2013; Le Blévec et al, 2017) gives the following auto-transiogram for the two facies

$$t_{11}(h) = t_{22}(h) = \frac{1}{2} + \frac{1}{\pi} \arcsin[\rho(h)], \tag{14}$$

Table 1 Notations for the truncated Gaussian model

p_i	Facies i proportion
$C_{ij}(h)$	Non centered covariance between facies i and j
$t_{ij}(h)$	Transiogram from facies i to facies j
T_{ij}	Transition rate from facies i to facies j
r_{ij}	Embedded transition rate from facies i to facies j
$\rho(h)$	Covariance of the latent standardized bi-Gaussian field $Z(x)$
q_1, q_2	Threshold of the Gaussian field $Z_1(x)$ and $Z_2(x)$
$g_{\rho(h)}$	Standardized bi-Gaussian density with correlation $\rho(h)$

and the cross-transiograms

$$t_{12}(h) = t_{21}(h) = \frac{1}{2} - \frac{1}{\pi}\arcsin[\rho(h)]. \tag{15}$$

For different facies proportions, the transiograms can be derived by numerical integration (Genz, 1992).

More than one bi-Gaussian function can also be used. This is the pluri-Gaussian (PGS) approach, which provides more flexibility thanks to a larger number of truncation rules. In this paper, two Gaussian functions are used, with two thresholds defining three facies i, j, k:

$$I_i(x) = 1, \quad I_j(x) = 0, \quad I_k(x) = 0 \text{ if } \quad Z_1(x) < q_1, \tag{16a}$$

$$I_i(x) = 0, \quad I_j(x) = 1, \quad I_k(x) = 0 \text{ if } \quad Z_1(x) \geq q_1, \quad Z_2(x) < q_2, \tag{16b}$$

$$I_i(x) = 0, \quad I_j(x) = 0, \quad I_k(x) = 1 \text{ if } \quad Z_1(x) \geq q_1, \quad Z_2(x) \geq q_2. \tag{16c}$$

As for TGS, the corresponding indicator statistical moments can be derived by numerical integration (Genz, 1992). Therefore, the facies transiograms can be derived from the parameters of the Truncated Gaussian model which are summarized in Table 1. A more detailed discussion on the link between the pluri-Gaussian parameters and the transiograms is given in Le Blévec et al (2017). This link is used in this paper to match different transiograms and a key objective is to develop covariance $\rho(h)$ such that the transiograms $t_{ij}(h)$ show rhythmicities and asymmetries.

2.3 Understanding cyclicity and rhythmicity with transiograms

Wilkinson et al (1997) define cyclicity as an apparent ordering between facies. Therefore, this definition directly relates to the transition rates (Eq. (6)) or the embedded transition rates (Eq. (9)) that define the juxtapositions between facies. For instance, the cyclic sequences of Figs. 1c and 1d have the upward embedded transition rate matrix

$$R = \begin{bmatrix} 0 & 1 & 0 \\ 0 & 0 & 1 \\ 1 & 0 & 0 \end{bmatrix}. \tag{17}$$

In other words, every facies transitions into only one other facies upwards ($r_{ij} = 1$). However, in practice such perfect facies successions are rare and the embedded transition rates generally do not equal one or zero but have intermediate values. For instance the sequences of Figs. 1a and 1b show two identical cycles while the other facies transitions are different. Such sequences can be called pseudo-cyclic. The limit behaviour, when the sequence is acyclic, happens if facies have equal probability of transitioning with the other facies, which would give for three facies the embedded transition rate matrix

$$R = \begin{bmatrix} 0 & 0.5 & 0.5 \\ 0.5 & 0 & 0.5 \\ 0.5 & 0.5 & 0 \end{bmatrix}. \tag{18}$$

One can quantify cyclicity with the probability P_c to observe a given cycle above a given facies, which can be written in the case of three facies for the cycle composed of facies 1-2-3-1 (under the Markov assumption of independence)

$$P_c = r_{12}\ r_{23}\ r_{31}. \tag{19}$$

We see that the notion of cyclicity is related to asymmetry by using the closing relations of transiogram matrices

$$P_c = r_{12}\ (1 - r_{21})\ \frac{T_{11}\ p_1 - r_{21}\ T_{22}\ p_2}{T_{33}\ p_3}, \tag{20}$$

as the probability P_c increases if the difference between r_{21} and r_{12} increases. Therefore, for a sequence with three facies, asymmetry between two facies results in cyclicity. The cyclicity studied here (Figs. 1c and 1d) is such that facies appear only once per cycle. This is incompatible with symmetric cycles that are not considered here. It also means that every facies tends to transition to one facies in the upward direction (Eq. (17)) and another one in the downward direction (which is why asymmetry plays an important role).

Rhythmicity is defined by the repetition of a facies at constant intervals. This is usually observed by computing variograms or transiograms on sequences that show dampened hole-effects (Journel and Froidevaux, 1982; Johnson and Dreiss, 1989; Ma et al, 2009). Rhythmicity cannot be quantified by embedded transition rates as they are independent of facies thicknesses. Rhythmicity can first be understood when studying two facies. If those facies have constant thicknesses, the auto-transiogram increases and decreases rhythmically with a wavelength that is equal to the sum of the two facies thicknesses (Jones and Ma, 2001). This is similar with more facies as we can still regard this as the succession of two facies, the one of interest and the one defined as everything that is not the facies of interest. This is interesting to consider in combination with cyclicity because the resulting sequences show a constant cycle thickness (Fig. 1d). Thicknesses along sequences are not usually constant but can show low variability which results in pseudo-rhythmicity and dampened hole-effects. The method developed here models pseudo-cyclic and pseudo-rhythmic sequences, quantified by transiograms.

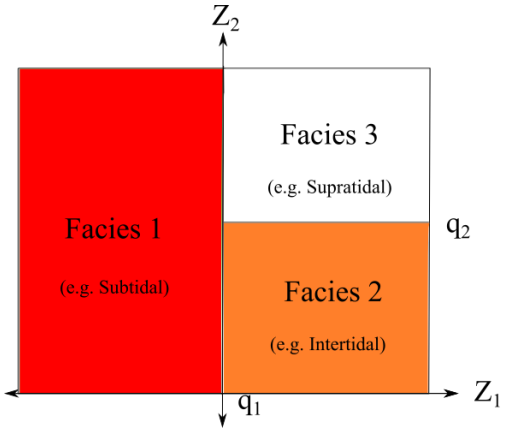

Fig. 2 Truncation rule used for the cyclical pluri-Gaussian simulation. q_1 and q_2 are the thresholds of the Gaussian functions $Z_1(x)$ and $Z_2(x)$

3 The cyclical Pluri-Gaussian approach

In this section, the classical Pluri-Gaussian Simulation is extended to render cyclicity (or asymmetry) (Sect. 3.1), rhythmicity (Sect. 3.2) and separable anisotropy (Sect. 3.3). The first two sections (Sect. 3.1, Sect. 3.2) present results in one dimension and the last section (Sect. 3.3) extends them to three dimensions.

3.1 Modelling asymmetrical facies juxtapositions in vertical successions

A method to simulate asymmetrical facies successions is summarized here (see Le Blévec et al (2017) for a detailed treatment). For simplicity two standardized bi-Gaussian random functions with a Cartesian truncation rule are used (Fig 2) as in Eq. (16). The correlation between the Gaussian functions $Z_1(x)$ and $Z_2(x)$ is based on the linear model of coregionalization (Wackernagel, 2013) with a shift α between the Gaussian functions as proposed by Armstrong et al (2011)

$$\begin{cases} Z_1(x) = Y_1(x), \\ Z_2(x) = \frac{\rho}{\rho_1(\alpha)} Y_1(x+\alpha) + \sqrt{1 - \frac{\rho^2}{\rho_1(\alpha)^2}} Y_2(x), \end{cases} \tag{21}$$

with $Y_1(x)$ and $Y_2(x)$ uncorrelated standardized bi-Gaussian functions, $\rho_1(h)$ the covariance of $Y_1(x)$ and ρ the resulting correlation coefficient between $Z_1(x)$ and $Z_2(x)$. The Gaussian function $Y_2(x)$ is defined by a covariance model $\rho_2(h)$.

The resulting transiograms between facies can be computed by Gaussian integral on the facies domain defined by the truncation rule as in Eq. (13). Le Blévec et al (2017) demonstrate analytically and numerically that these

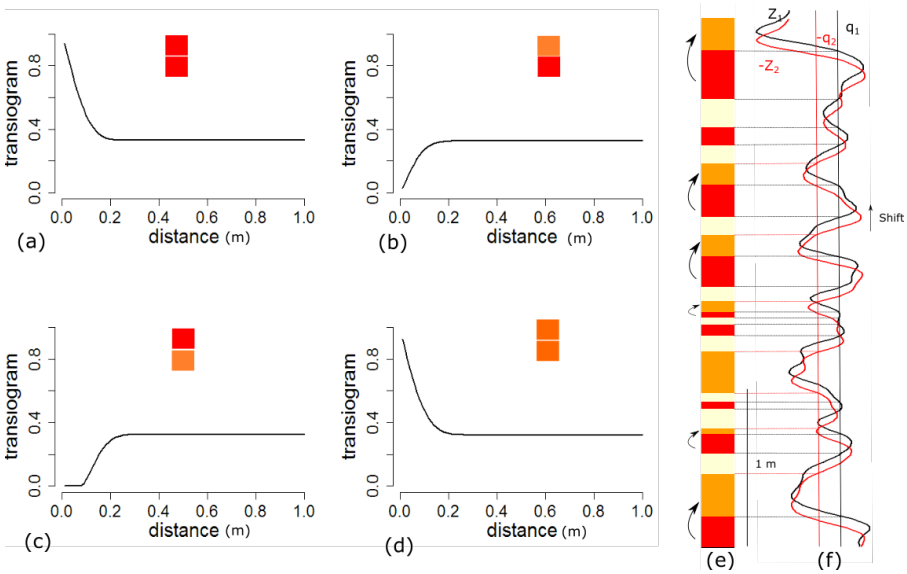

Fig. 3 One realization (e) with corresponding transiogram matrix model (a-d) and Gaussian functions $Z_1(x)$ and $Z_2(x)$ (f). Parameters: $\rho = -0.8$, $r_1 = r_2 = 0.1$, $\alpha = 0.05$, $p_1 = p_2 = p_3$

transiograms are asymmetric as in Eqs. (4) and (7). A sensitivity study is also carried out on the parameters α and ρ showing that the asymmetry can be controlled by varying these two parameters. Here, the covariance models $\rho_1(h)$ and $\rho_2(h)$ used for the Gaussian functions $Y_1(x)$ and $Y_2(x)$ are Gaussian

$$\rho_1(h) = \exp(-\frac{h^2}{r_1^2}), \tag{22a}$$

$$\rho_2(h) = \exp(-\frac{h^2}{r_2^2}), \tag{22b}$$

with parameters r_1 and r_2 the ranges of the models. An example of a vertical sequence generated with this method and the corresponding facies transiograms is shown in Fig. 3. The simulation method of the latent Gaussian functions is given in Sect. 4 and the transiograms are computed numerically (Genz, 1992) based on Eq. (13). Only four transiograms instead of nine are shown for the three facies (Figs. 3a, 3b, 3c and 3d), because the third facies can be considered as the background and its transiograms can be directly deduced from the transiograms of the other facies.

It is clear from Fig. 3 in the realization that the facies are statistically organized in shallowing upward cycles as highlighted by the low tangent at the origin of the cross transiogram from intertidal (orange) facies to subtidal (red) facies upwards (Fig. 3c). Indeed, this transition is absent along the vertical section while the opposite transition (from subtidal facies to intertidal facies) occurs 6 times. However, the succession is not completely cyclic

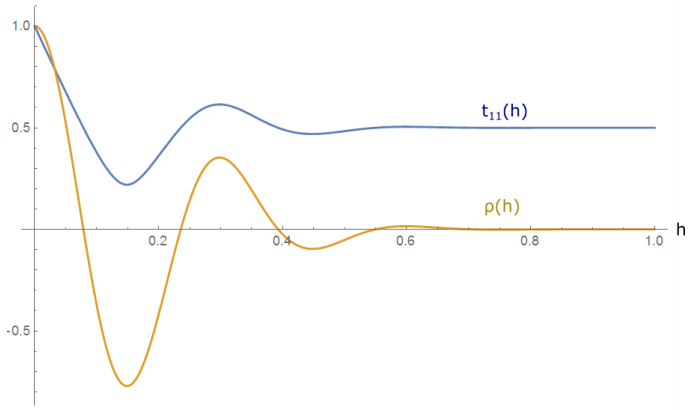

Fig. 4 Hole-effect on the latent Gaussian field (yellow, Eq. (23)) and the resulting hole-effect on the facies transition probability (blue, Eq. (24)), with $r_1 = 0.3$ and $b_1 = 20$.

(Fig. 3e) because of a low but non-null probability of the subtidal (red) facies to transition upwards directly to the supratidal (white) facies. A high variation of facies thicknesses is also noted, resulting in a non-rhythmic sequence.

3.2 Modelling rhythmicity in vertical successions

Using covariance functions with rhythmicity for the latent Gaussian field is expected to produce facies transiograms with rhythmicities. This hypothesis is verified in this section in which a new indicator transiogram model representing facies rhythmicity is defined. In one dimension, the cosine function is a valid covariance model (Chiles and Delfiner, 2012) and produces by truncation vertical sequences with a constant cycle thickness. As this is rarely observed, a model in which the oscillations attenuate with distance, called dampened hole-effect (Pyrcz and Deutsch, 2014) gives more flexibility in reproducing cycle thicknesses. Ma and Jones (2001) define the Gaussian cosine covariance as the product of two valid covariance functions

$$\rho(h) = \exp(-\frac{h^2}{r^2}) * \cos(b\ h). \tag{23}$$

This covariance gives dampened oscillations controlled by the two parameters r and b. If the parameter r tends to infinity, the model is the cosine function. According to Eq. (14) the resulting hole-effect transiogram model is

$$t_{11}(h) = \frac{1}{2} + \frac{1}{\pi} \arcsin[\exp(-\frac{h^2}{r^2}) * \cos(b\ h)]. \tag{24}$$

As seen in Fig. 4, this transiogram model has a similar wavelength as the latent covariance model (Eq. (23)) and the attenuation of the oscillations is

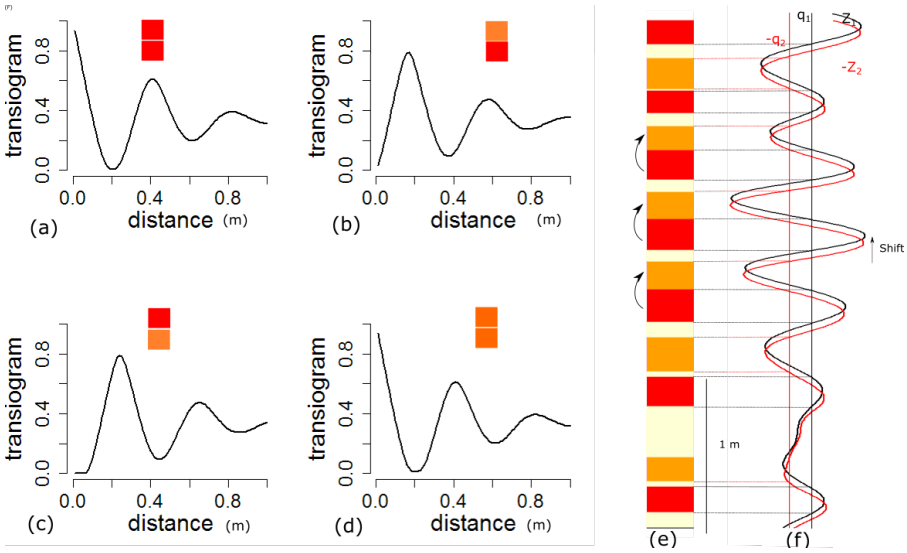

Fig. 5 One realization (e) with transiogram matrix model (a-d) and latent Gaussian functions (f) with parameters: $\rho = -0.82$, $r_1 = r_2 = 0.6$, $b_1 = 15$, $b_2 = 30$, $\alpha = 0.04$, $p_1 = p_2 = p_3$

also similar. Therefore, this transiogram model seems a good candidate to model rhythmicity because of its flexibility.

It is important to remember that Eq. (24) is valid only if the threshold is zero, that is the two facies have equal proportions. When this is not the case, the model $t_{11}(h)$ can be numerically computed (Genz, 1992). Figure 5 gives the simulation of a vertical sequence with three facies (Fig. 5e) and corresponding hole-effect transiograms (Figs. 5a, 5b, 5c and 5d). The covariances of the two Gaussian fields have the form of Eq. (23) with respective parameters r_1, b_1 and r_2, b_2.

Figure 5 clearly shows the effect of rhythmicity on the transiograms and the corresponding realization. The facies cycles are repeated in the vertical succession (Fig. 5e) with a rhythmicity controlled by the latent Gaussian functions (Fig. 5f). More specifically, it seems that the cycle thickness approximately equals the wavelength of the latent Gaussian function (Figs. 5e and 5f). Asymmetry in facies stacking is also combined with rhythmicity to create a cyclical vertical succession. After developing covariance models in one dimension, it is necessary to expand these models into two and three dimensions while incorporating anisotropy.

3.3 Modelling facies distributions in two and three dimensions with separable anisotropy

In sedimentary deposits, a strong anisotropy is always observed between the vertical direction and the one parallel to stratigraphy. A simple way to rep-

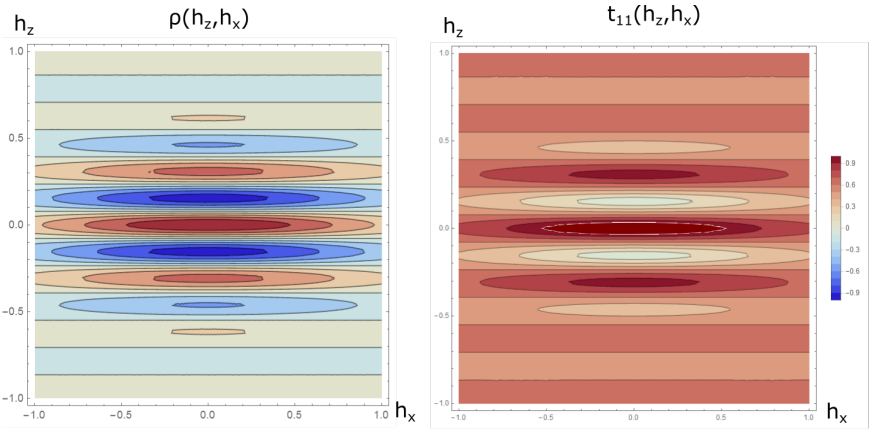

Fig. 6 Covariance map of the latent Gaussian function (left, Eq. (26)) and resulting transiogram (right, Eq. (27)) in two dimensions with $r_z = 0.5$, $r_x = 1$ and $b = 20$

resent such anisotropy is to use a separable covariance (Chiles and Delfiner, 2012). A separable covariance model can be built from the product of a covariance in the vertical direction $\rho_v(h_z)$ and a covariance along stratigraphy $\rho_l(h_x, h_y)$

$$\rho(h_x, h_y, h_z) = \rho_l(h_x, h_y) * \rho_v(h_z). \tag{25}$$

As hole-effect usually occurs only in the vertical direction, it is possible to use a dampened hole-effect model for $\rho_v(h_z)$ (Eq. (23)) but not for $\rho_l(h_x, h_y)$

$$\rho(h_x, h_y, h_z) = \exp[-\frac{h_x^2}{r_x^2} - \frac{h_y^2}{r_y^2}] * \exp[-\frac{h_z^2}{r_z^2}] \ \cos[b\ h_z]. \tag{26}$$

Along stratigraphy, a standard geometrical anisotropy (which is also separable in this case of a Gaussian covariance) is here used (Chiles and Delfiner, 2012). The principal directions of anisotropy can also be changed by rotations (Chiles and Delfiner, 2012). According to Eq. (14), the corresponding transiogram model of two facies, after thresholding a single Gaussian at cut off 0 is therefore

$$t_{11}(h_x, h_y, h_z) = \frac{1}{2} + \frac{1}{\pi} \arcsin \left[\exp[-\frac{h_x^2}{r_x^2} - \frac{h_y^2}{r_y^2}] * \exp[-\frac{h_z^2}{r_z^2}] \ \cos[b\ h_z] \right]. \tag{27}$$

Equation (27) shows that even though the covariance of the latent Gaussian field is separable, the resulting transiogram is not separable. Figure 6 compares values (h_y constant) of the latent Gaussian function covariance and the resulting transiogram which both show a dampened hole-effect in the vertical direction and the absence of a hole-effect along stratigraphy. In intermediate directions, the dampened hole-effect is present but more attenuated. Once again, the behavior of the transiogram in two or three dimensions is very similar to the covariance of the latent variable. This suggests that there is about as much flexibility in the transiogram model as in the covariance model.

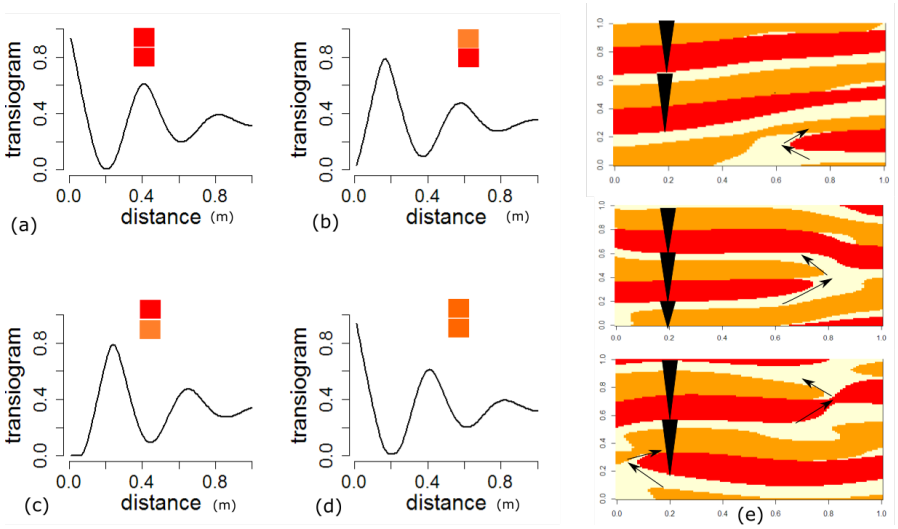

Fig. 7 Vertical transiogram matrix model (a-d) and three corresponding realizations (e). $\rho = -0.8$, $r1_z = 0.6$, $r1_x = r1_y = 0.4$, $b_1 = 15$, $b_2 = 30$, $r2_z = 0.6$, $r2_x = r2_y = 0.4$, $\alpha = 0.04$

These transiogram models are valid for two facies in equal proportions but for a more general case, different examples in three dimensions are shown in cross sections with their corresponding transiograms in the vertical direction (Figs. 7 and 8). The transiograms have been computed by numerical integration (Genz, 1992) of a Gaussian density (Eq. (13)). The parameters for the two Gaussian functions are respectively $r1_x$, $r1_y$, $r1_z$ and $r2_x$, $r2_y$, $r2_z$, and vertical hole-effect parameters b_1, b_2.

Figure 7 shows the combination of asymmetry, rhythmicity and anisotropy in facies distributions in both the realizations and the transiograms. The facies are ordered according to the asymmetry: subtidal, intertidal and supratidal facies upwards (Fig. 7e). The vertical thickness of these cycles is almost constant, confirming the rhythmicity. The different realizations can be interpreted as facies beds that pinch out laterally or split into different cycles and inter-finger.

Changes in the different parameters can create more complex transiogram models. By using a hole-effect covariance on the second Gaussian function but not on the first, only the orange facies auto-transiogram shows the combined effect of the Gaussian covariance and the hole-effect covariance (Fig. 8d). This results in more complex geometries for the orange and white facies that show two combined behaviors. They show thin beds corresponding to the high frequency rhythmicity and thicker beds (Fig. 8e) corresponding to a lower frequency. The red facies has a different transiogram from the other facies (Fig. 8a), and appears to truncate both of them. Bodies of the red facies can be interpreted either to have erosional boundaries or to be diagenetic in origin, having formed after deposition. In order to have a better understanding

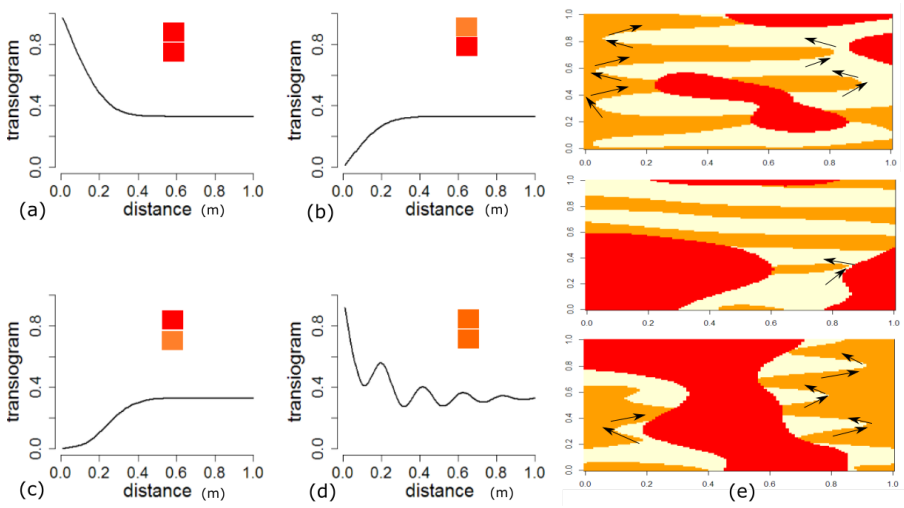

Fig. 8 Vertical transiogram matrix model (a-d) and three corresponding realizations (e). $\rho = -0.6$, $r_{1_z} = 0.2$, $r_{1_x} = r_{1_y} = 0.4$, $b_1 = 0$, $b_2 = 30$, $r_{2_z} = 0.6$, $r_{2_x} = r_{2_y} = 0.4$, $\alpha = 0.1$

of the geometries generated by this transiogram model (Fig. 8), a three dimensional simulation with the same transiograms is also presented in Fig. 9. The orange and white facies clearly show vertical rhythmicity with low lateral variability in thickness, consistent with a depositional architecture, while the red (diagenetic) facies truncates them.

Until now Gaussian covariances have been used. However, a more general model could be used in order to control the behaviour of the transiogram at the origin. For instance, using the stable covariance model (Chiles and Delfiner, 2012) with a geometrical anisotropy along stratigraphy and separable anisotropy in the vertical direction would give transiograms of the form (for one latent Gaussian function with a threshold at zero)

$$t_{11}(h_x, h_y, h_z) = \frac{1}{2} + \frac{1}{\pi} \arcsin \left[\exp \left[-\left(\sqrt{\frac{h_x^2}{r_x^2} + \frac{h_y^2}{r_y^2}} \right)^{\beta} \right] * \exp[-(\frac{h_z}{r_z})^{\gamma}] \, cos[b\, h_z] \right]. \tag{28}$$

The smoothness of facies boundaries decreases with the coefficients β and γ ($0 < \beta, \gamma \leq 2$).

4 Conditional simulation of the cyclical Pluri-Gaussian model

A simple method is here presented to simulate the latent Gaussian functions with covariance presented in Sect. 3 and to condition them to the facies observed along the wells.

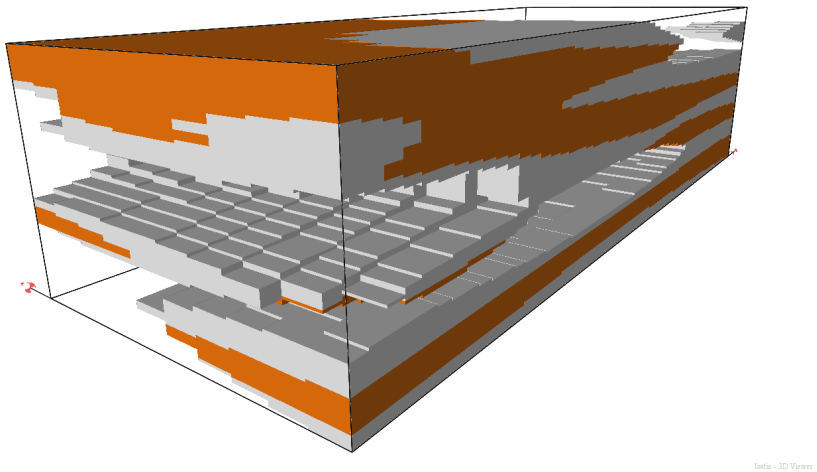

Fig. 9 Three dimensional simulation with the cyclical PGS obtained with the parameters shown in Fig. 8. The void represents the red facies in Fig. 8

4.1 Unconditional simulation

The continuous spectral approach developed by Shinozuka (1971) is convenient to build simulations based on separable covariances. The Fourier transform of the covariance model is normalized and used as a probability density function (pdf) to sample frequencies ν_k generating the Gaussian field

$$Z(x) = \sqrt{\frac{2}{N}} \sum_{k=1}^{N} cos(< \nu_k, x > + \Phi_k), \tag{29}$$

with Φ_k random phases sampled from a uniform pdf between 0 and 2π and $<>$ the scalar product. The resulting field is Gaussian (central limit theorem) when N tends to infinity. Based on the knowledge of x, the individual value of $Z(x)$ at each location x can be simulated, which enables the algorithm to be coded in parallel and to be grid-free.

The spectral approach is well suited for a separable covariance as the multi-dimensional Fourier transform of a separable covariance is the product of the Fourier transforms. The three dimensional Fourier transform of a separable covariance model $\rho(h_x, h_y, h_z)$ (Eq. (25)) is

$$\mathcal{F}_{\rho(h_x,h_y,h_z)}(\nu_z, \nu_x, \nu_y) = \mathcal{F}_{\rho_v(h_z)}(\nu_z) \;\; \mathcal{F}_{\rho_l(h_x,h_y)}(\nu_x, \nu_y), \tag{30}$$

which means the frequencies ν_z in the vertical direction are sampled independently from ν_x and ν_y according to the Fourier transform of their respective covariance models.

In order to simulate the covariance model of Eq. (26), the Fourier transforms of the covariance in the vertical direction and the lateral plane need to be found (Eq. (30)). For the lateral plane, as a Gaussian covariance with geometrical anisotropy is also separable, the two directions h_x and h_y are sampled independently

$$\mathcal{F}_{\rho(h_x,h_y)}(\nu_x,\nu_y) = \mathcal{F}_{\rho_v(h_x)}(\nu_x) \;\; \mathcal{F}_{\rho_l(h_y)}(\nu_y). \tag{31}$$

The Fourier transform of a Gaussian covariance is a Gaussian pdf (Chiles and Delfiner, 2012). Thus, the Fourier transforms in the lateral direction h_x and h_y are respectively $\mathcal{N}(0, \frac{\sqrt{2}}{r_x})$ and $\mathcal{N}(0, \frac{\sqrt{2}}{r_y})$. In the vertical direction, the Fourier transform of the Gaussian cosine covariance model (Eq. (23)) is a bi-modal Gaussian pdf $\mathcal{N}(b, \frac{\sqrt{2}}{r_z}) \cup \mathcal{N}(-b, \frac{\sqrt{2}}{r_z})$ (by modulation of the cosine function)

$$\mathcal{F}_{\rho_z(h_z)}(\nu_z) = \frac{1}{2\; r_z\sqrt{\pi}} \left[\exp(-\frac{1}{4}\frac{(b+\nu_z)^2}{r_z^2}) + \exp(-\frac{1}{4}\frac{(b-\nu_z)^2}{r_z^2}) \right]. \tag{32}$$

Algorithm 1 describes how to simulate a facies field with such a covariance model. Figure 10 shows experimental variograms $(1-\rho(h))$ of 10 realizations of the simulation of a separable Gaussian cosine covariance in two dimensions (Eq. (26)). As expected the covariances of the realizations are centered around the covariance model and represent the hole-effect only in the vertical direction. Some fluctuations of the experimental variograms on the realizations are observed (Fig. 10) which are explained in detail by Lantuéjoul (1994) or Emery and Lantuéjoul (2006).

Algorithm 1 Separable Gaussian cosine simulation in three dimensions

1: $\phi \longleftarrow$ Generate N samples in $\mathcal{U}(0, 2\pi)$
2: $\nu_z \longleftarrow$ Generate N samples in $\mathcal{N}(b, \sqrt{2}/r_z)$
3: $\nu_x \longleftarrow$ Generate N samples in $\mathcal{N}(0, \sqrt{2}/r_x)$
4: $\nu_y \longleftarrow$ Generate N samples in $\mathcal{N}(0, \sqrt{2}/r_y)$
5: $i \longleftarrow$ Generate N samples in $(-1, 1)$ to be multiplied with ν_z
6: For every location (x, y, z): apply Eq. (29)
7: Truncation according to proportions

The spectral approach can also be used to simulate a stable separable covariance model (Eq. (28)). The Fourier transform of a stable covariance is a stable spectral pdf with stability and scale parameters α and r, skewness and location 0 (Chiles and Delfiner, 2012). Therefore, to simulate this covariance, one can use Algorithm 1 by replacing the Gaussian distributions with the stable distributions. These simulations are unconditional, and they must now be conditioned to facies data observed at specific locations in the simulated volume.

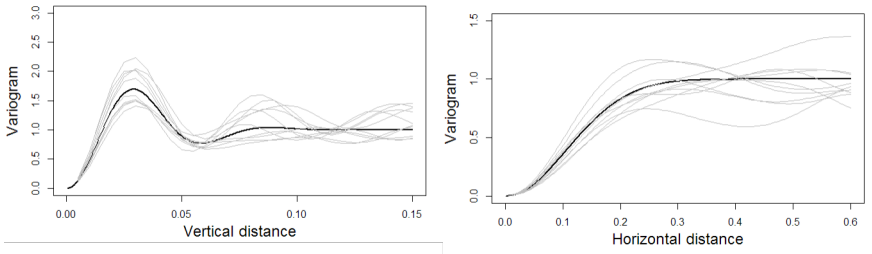

Fig. 10 Variograms (grey) computed from ten realizations with model (black) and parameters: r_x=0.15, r_z=0.05, $b = 100$, $N = 100$. The simulated grid has $200 * 200$ cells of size $(0.005, 0.005)$

4.2 Conditioning the Gaussian simulation to facies data

Some methods already exist for conditioning pluri-Gaussian simulations (Chiles and Delfiner, 2012; Emery and Lantuéjoul, 2006). This section summarises the main steps and proposes improvements in the case of separable covariances. The truncation rule defines intervals of the Gaussian function corresponding to each facies. At data locations x_i, the observed facies constrain the Gaussian function with inequalities of the form

$$q_i < Z(x_i) < q_i', \tag{33}$$

with q_i and q_i' being the thresholds associated with the truncation diagram. The conditional simulation is usually performed in three steps (Chiles and Delfiner, 2012). First, an unconditional simulation $Z^u(x)$ is performed as in Sect. 4.1. Then, a local conditional simulation of $Z(x_i)$ is carried out only at data locations x_i using Gibbs sampling such that Eq. (33) is respected (Freulon and de Fouquet, 1993). Finally, simple kriging $R(x)$ is calculated for the difference at data locations between the conditional and unconditional simulation

$$R(x_i) = Z(x_i) - Z^u(x_i), \tag{34}$$

is performed (Chiles and Delfiner, 2012)

$$R(x) = \sum_i \lambda_i(x)\ R(x_i), \tag{35}$$

with $\lambda_i(x)$ the kriging weights (Chiles and Delfiner, 2012). Therefore, the conditional Gaussian function Z at every location x is finally obtained by

$$Z(x) = Z^u(x) + R(x). \tag{36}$$

The Gibbs sampling at data locations is not described here. Any algorithm can be chosen (Emery et al, 2014) and applied with the desired covariance model to simulate the values of $Z(x_i)$ at the data locations. However, the kriging of the difference (Eq. (35)) can be optimized when using a separable covariance such as the model of Eq. (25). This is important because kriging

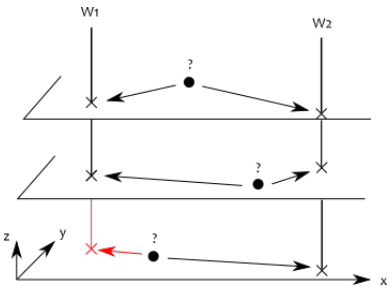

Fig. 11 The screening effect for simple kriging applied on two wells W_1 and W_2 to estimate three locations on three different horizontal planes with one extended well (red)

over the whole domain is computationally expensive, and can make simulation prohibitively slow. The simple kriging is optimized thanks to the well known screening properties of separable covariances (Chiles and Delfiner, 2012). With a separable anisotropy between the vertical direction and the lateral plane, such as with the covariance model of Eq. (25), the weights $\lambda_i(x)$ associated with data located on different lateral planes from that of the estimated location x are equal to zero (Chiles and Delfiner, 2012). This means that the estimation of a location only depends on the data at the same horizontal level, and the number of kriging weights therefore equals the number of wells intersecting this horizontal level, as shown in Fig. 11. Assuming all wells are vertical and have the same length, the number of weights for every kriged point is therefore the number total of wells. If this is not the case, for instance because some vertical wells do not penetrate a particular level, it is convenient to artificially extend them by an unconditional simulation with Gibbs sampling (Fig. 11), so that the geometrical configuration of the data points remains the same at all levels. Therefore, the weigths are the same for every horizontal plane and the dual form of two-dimensional kriging may be used, in which the data covariance matrix is inverted only once (Chiles and Delfiner, 2012). This enables rapid and efficient kriging.

In this paper, with the two latent Gaussian functions to condition (Eq. (21)) and the truncation rule of Fig. 2, the two conditions at each data point are

$$Z_1(x_i) < q_{1_i} \qquad Z_2(x_i) < q_{2_i}. \tag{37}$$

The conditioning procedure is successively performed for the two uncorrelated Gaussian function Y_1 (which equals Z_1) and Y_2. As Z_2 depends on Y_1 (Eq. (21)) the thresholds for Y_2 depend on the values simulated for Y_1, which are given by solving Eq. (21)

$$Y_2(x_i) < \frac{q_{2_i} - \frac{\rho}{\rho_{Y_1(\alpha)}} Y_1(x_i + \alpha)}{\sqrt{1 - \frac{\rho^2}{\rho_{Y_1(\alpha)^2}}}}. \tag{38}$$

An example of conditional simulation with this method is given in the following section.

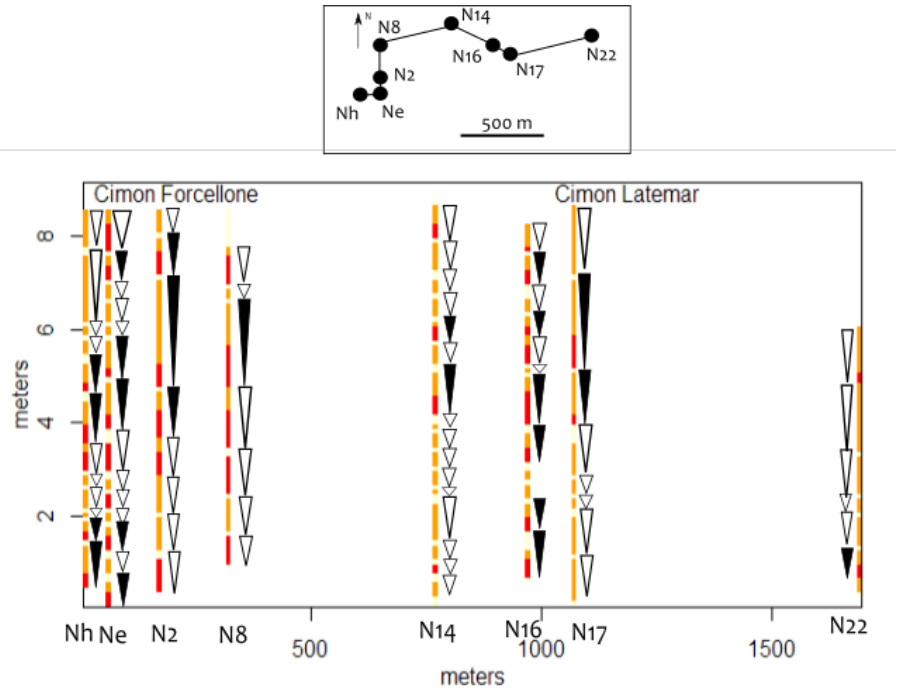

Fig. 12 Logs through the Upper Cyclic Facies interval of the Latemar carbonate platform (Peterhänsel and Egenhoff, 2008) subtidal (red), intertidal (yellow) and supratidal (white)

5 Case study: the Latemar carbonate platform, northern Italy

The Triassic Latemar carbonate platform is superbly exposed in northern Italy and has been chosen as a case study as it provides well-documented examples of facies cyclicity with rhythmicity and asymmetry in shallow-marine peritidal strata (e.g. Goldhammer et al (1990)). Rhythmicity has been quantified along a vertical sequence through the entire platform succession using spectral analysis, in order to understand the potential expression of orbital forcing (Milankovitch cycles) on platform growth (Hinnov and Goldhammer, 1991; Preto et al, 2001). However, few studies describe sequences in different parts of the platform with the aim of performing facies modelling. Here, the dataset of Peterhänsel and Egenhoff (2008) (Upper Cyclic Facies stratigraphic interval) is used to evaluate and model asymmetrical (upward-shallowing) facies cycles and facies rhythmicity near the topographically high platform margin (Cimon Latemar) and in deeper lagoonal deposits of the platform interior (Cimon Forcellone). They describe five microfacies based on thin sections: peloidal packstone to wackestone (1), algae peloidal packstone (2), fenestral packstone to wackestone (3), packstone to grainstone (4), diagenetically overprinted grainstone to packstone (5). To illustrate our geostatistical method, these microfacies are re-grouped into three main environments of deposition:

subtidal (facies 1), intertidal (facies 2 and 3), supratidal storm deposits (facies 4 and 5). The next paragraph provides a quantitative analysis of the variations of these three facies.

5.1 Qualitative and quantitative study of the case-study dataset

As illustrated by Fig. 12, the eight vertical logs show a high number of facies transitions. The asymmetry is clear as the subtidal facies (red) tends to be on top of the supratidal (white) facies. However, complete upward-shallowing facies cycles, containing subtidal, intertidal and supratidal deposits, occur only 24 times, while there are 56 incomplete cycles in the eight logs, which means that the sequences are pseudo-cyclic. The subtidal facies appears to show regular spacing between beds within some wells (Fig. 12, in logs N8 and N16), which would suggest a pseudo-rhythmicity of this facies. This is not the case for the intertidal and supratidal facies, which show very different spacings between the beds (Fig. 12).

All this information can be verified in the experimental transiograms computed on the logs (Fig. 13, grey points). A dampened hole effect is observable on the auto-transiogram of the subtidal deposits (Fig. 13a). The tangent at the origin of the cross-transiogram of intertidal deposits overlain by subtidal deposits (Fig. 13c) is low, showing that this transition is rare. More precisely, $T_{12} = 2.06$ and $T_{21} = 0.19$ which means according to Eq. (7) that the intertidal facies is four times more likely to overlie the subtidal facies than to underlie it. Moreover, $P_c \approx 0.3$, which clearly shows that the transitions between facies are pseudo-cyclic.

5.2 Inference of the co-regionalization model

As seen in Fig. 13a, the subtidal deposit auto-transiogram shows a dampened hole effect. In order to model this hole effect properly, it is easier to derive it from only one covariance rather than a combination of two covariances. Therefore, the truncation rule of Fig. 2 where the subtidal facies is defined by only one Gaussian function, is chosen. The use of more complex truncation rules is discussed in Sect. 6.1.

The parameters of the pluri-Gaussian model are determined using the procedure described in Le Blévec et al (2017). Only the auto- and cross-transiograms of two of the three facies are necessary to determine the parameters of the model, as the transiograms for the third facies are derived from those of the two other facies. A trial and error procedure is here chosen for determining the parameters, as this gives the possibility to incorporate conceptual knowledge. For instance, as it is known that rhythmicity and asymmetry occur, it is important to incorporate these features during the model construction, which would be difficult with an automatic fitting procedure.

The covariance of the first Gaussian function $\rho_1(h)$ is used to describe the transiogram of the subtidal facies. The Gaussian cosine model (Eq. (23))

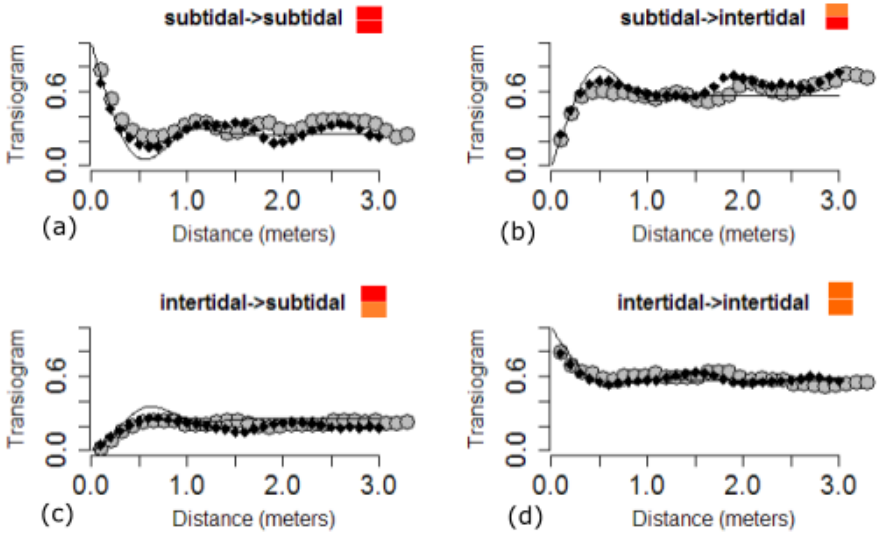

Fig. 13 Experimental transiograms (grey points), model (black line) and realization (black diamonds) after simulation with parameters in Table 2

gives an appropriate fit although the oscillations observed on the logs seem less pronounced (Fig. 13a). This could be improved by using a more complex covariance model and is discussed in Sect. 6.2. Then, the correlation coefficient ρ and the shift α can be chosen to fit the transition rates between the subtidal and intertidal facies. Here the asymmetry (Eq. (7)) is clear, because the probability of facies intertidal overlying facies subtidal is four times higher that of the opposite. Therefore, the shift α is equal to the size of one vertical cell and the correlation coefficient ρ is rather high (-0.6) which allows the model to match these transition rates. The shift is strictly vertical because no information on a possible lateral asymmetry is available (this topic is further discussed in Sect. 6.3). Finally the covariance of the second Gaussian functions $\rho_2(h)$ determines the transiogram of intertidal facies. A rhythmic covariance is not necessary here, as the transiogram does not show a clear hole effect. There is not enough information to determine the lateral ranges of the covariance directly from the data. Therefore, they are derived from visual comparison of the realizations with the outcrop facies panel interpreted between the vertical logs by Peterhänsel and Egenhoff (2008) and are chosen to be isotropic (in the lateral plane). Finally, the thresholds q_1 and q_2 of the Gaussian functions are determined according to the proportions of the facies and the correlation coefficient ρ between the two Gaussian random functions (Armstrong et al, 2011). The parameters are summarized in Table 2.

Vertically, a Gaussian cosine covariance is chosen but laterally an exponential covariance (Chiles and Delfiner, 2012) is used as the Gaussian covariance can cause numerical issues. A Gaussian or cubic covariance in the lateral direction leads to a singular kriging system for the conditioning step as the

Table 2 Parameters of the Pluri-Gaussian simulation for the Latemar platform

(q_1, q_2)	$(-0.65, 0.41)$	Thresholds for the two Gaussian functions
ρ	-0.6	Correlation between Gaussian functions
α	$0.1m$	Vertical shift between Gaussian functions
$(r_{1_x}, r_{1_y}, r_{1_z})$	$(500m, 500m, 0.8m)$	Range of the first Gaussian covariance
$(r_{2_x}, r_{2_y}, r_{2_z})$	$(500m, 500m, 0.4m)$	Range of the second Gaussian covariance
(b_1, b_2)	$(5m^{-1}, 0m^{-1})$	Vertical frequencies of the two covariances

lateral range is large (Sect. 4.2). A stable covariance with a power close to two could also be chosen to obtain a smoother model than that obtained with the exponential.

5.3 Simulation results

The cell sizes of the grid are 0.1 meters vertically and 10 meters laterally in both North and East directions, which gives approximately 800,000 cells. The simulation takes approximately one minute to run with a standard Intel processor i7, but it could be much faster by performing a parallel unconditional simulation with the spectral method, which is the longest computational step. The conditioning by kriging every surface independently, as described in Sect. 4.2, is almost instantaneous. One realization of the field is shown in Fig. 14.

The visual aspect of the simulation is granular due to the exponential covariance model used in the lateral plane. Visually, the subtidal (red) facies tends to lie on top of the supratidal (white) facies and rhythmicity is confirmed by the regular thickness between two subtidal (red) facies bodies. The transiograms of the wells and the transiograms computed on one realization are compared in Fig. 13. The sills derived from simulation (black diamonds in Fig. 13) are accurate, which means that the facies proportions match those in the wells. The tangent at the origin of the auto-transiograms is appropriately fitted, which means the average thicknesses of different facies bodies honours the well data. The tangent at the origin of the cross-transiograms matches the transition rates of the wells ($T_{12} = 2.1$ and $T_{21} = 0.19$) which means the asymmetry is respected. The hole effect in the realization transiogram is less pronounced that the one used for the model, but is closer to the one observed at the wells (grey circles in Fig. 13). This might be due to the conditioning to the wells, where the experimental transiograms show less pronounced oscillations (black lines in Fig. 13).

6 Discussion

In order to illustrate the method, standard parameters have been chosen so far for both the synthetic examples and the case study. However, some parameters

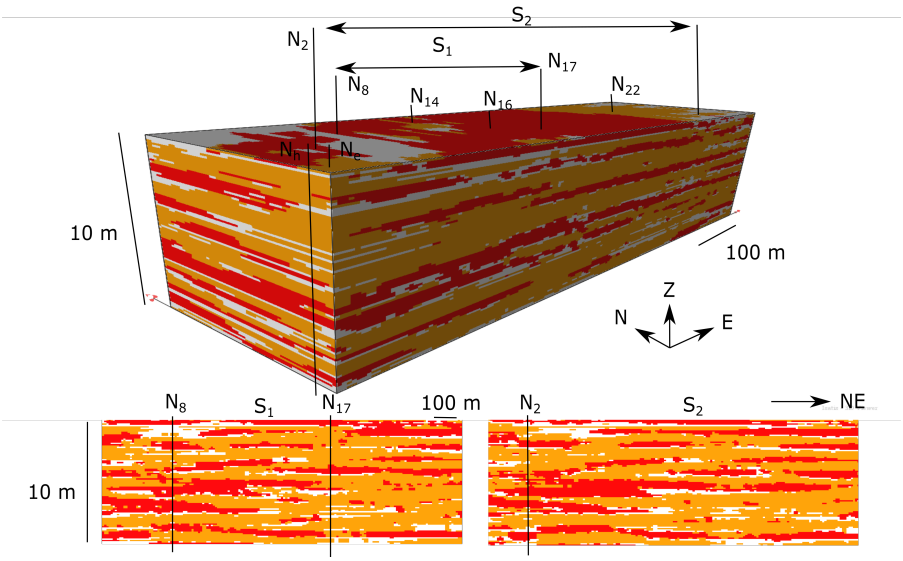

Fig. 14 One realization of the Latemar facies field from Peterhänsel and Egenhoff (2008) data (Fig. 12), and two cross-sections obtained with the parameters summarized in Table 2

such as the truncation rule, the covariance model, or the shift can be made more complex to adjust to different geological environments.

6.1 The truncation rule

6.1.1 Choosing the truncation rule

The same truncation rule has been applied through the paper (Fig. 2) with the subtidal facies defined by the first Gaussian function and the two others by both Gaussian functions. This has implications for the geometries of individual facies bodies and for facies relationships. The facies defined by the first Gaussian function erodes the two other facies (e.g. Fig. 8e), which means that bodies of these facies can have very different geometries those of the other facies. This behaviour can be reduced by increasing the correlation ρ between the two Gaussian functions $Z_1(x)$ and $Z_2(x)$.

The truncation rule affects not only the facies transiograms but also higher order statistical moments, which can have an impact on connectivity (Beucher and Renard, 2016). However, these moments are not known analytically and so are difficult to use for defining the truncation rule. It is recommended that the earth modeller tries different truncation rules and inspects the visual aspect of simulations so that it matches with his/her conceptual knowledge.

6.1.2 Adapting the truncation rule for more facies

In this paper, only three facies have been used to illustrate the method. Two methods for generalizing the truncation rule to more facies are found in the literature: either the truncation is made more complex (Galli et al, 2006) giving more deterministic relations between facies, or the number of Gaussian functions is increased (Maleki et al, 2016). The first method would be too limited to represent a large number of transition rates between facies, while the second one should be able to model all transition rates (but the number of parameters would be very high). The choice between the two methods should depend on the case study and further work on this topic is required. It should also be noted that some methods that create automatic truncation rules have been developed (Deutsch and Deutsch, 2014; Astrakova et al, 2015). It would be fruitful to generalize these methods by incorporating the shift between the Gaussian functions in order to match asymmetric transition probabilities.

6.2 Elaborating more complex hole-effect models

The vertical hole-effect model used in this paper is made of two parameters r_z and b (Eq. (23)) which provides some flexibility to match observed rhythmicity. However, the case study shows that the observed transiograms can be even more complex (Fig. 13) and two parameters might not be sufficient to represent them. The covariance model could be modified to incorporate more than one structure (Chiles and Delfiner, 2012). For instance a Gaussian covariance or a cosine covariance can be added to the Gaussian cosine model (Eq. (23)). The corresponding simulation can then be performed by summing together the uncorrelated Gaussian random functions associated with each nested structure of the covariance.

6.3 Walther's law

The method developed in this paper models cyclicity only in the vertical direction, which is consistent with observations of most outcrop and subsurface data. However according to Walther's law, the transitions between facies should be equivalent laterally and vertically (Middleton, 1973). This means that the facies ordering should be similar and the transition rates proportional as in Markov Chains methods (Doveton, 1994; Purkis et al, 2012). Thus vertical asymmetry should also be observed laterally. It is possible to model such patterns with the presented method by defining a shift between the Gaussian functions (Eq. (21)) with a lateral component, such that the asymmetry is also lateral (Renard and Beucher, 2012; Le Blévec et al, 2016).

This choice will depend on the depositional environments, processes, controls, and scale to be modelled. These aspects are typically interpreted with reference to an underlying conceptual model, such as those for allocyclically

and autocyclically generated facies cycles in peritidal carbonate strata (Pratt and James, 1986; Goldhammer et al, 1990). The facies architectures to be modelled are also scale dependent. Environments of deposition generally have large lateral extents (1 - 10 km), such that few lateral transitions between them are observed at reservoir (1 - 10 km) and interwell (<1 km) scales (Sena and John, 2013), which limits the expression of lateral ordering of depositional environments. At smaller scales, the lateral transitions between lithofacies within depositional environments (or facies associations) may be different from the vertical transitions (Hönig and John, 2015) because of erosion or lateral changes in palaeotopography. The resulting lithofacies distributions may be highly variable, potentially reflecting a facies migration that is well-ordered and obeys Walther's law as one end member (Obermaier et al, 2015) or more complex and less ordered facies mosaics as the opposite end member (Wilkinson et al, 1997). The choice of appropriate conceptual model at the scale of depositional environments (facies association) or lithofacies must be made by the earth modeler in collaboration with the geologist, and then used to govern the selection of parameters of the model.

7 Conclusion

While cyclicity and rhythmicity are commonly observed in geological data sets, few existing geostatistical algorithm can model both patterns in an efficient manner. By addressing this issue, the method developed here is promising for modelling carbonate or clastic reservoirs that contain such cyclical facies successions. Broadly speaking, cyclicity and rhythmicity are quantified by facies transiograms that are computed from data (e.g. vertical facies successions) and fitted with an advanced truncated Pluri-Gaussian model for performing three dimensional simulations.

The model used for the latent Gaussian functions is the linear model of coregionalization with a spatial shift, which creates the asymmetric cycles. The covariance of the Gaussian functions presents a dampened hole effect for capturing the rhythmicity. As this hole effect is generally observed only in the vertical direction, a separable covariance model, which is the product of a lateral and a vertical covariance is used so that no rhythmicity is modelled laterally along the stratigraphy. The space-time separable covariance is simulated readily by the continuous spectral method. The numerical properties of separable covariance allows rapid and efficient conditioning to data via kriging of every horizontal surface independently. The procedure has been applied successfully to model a carbonate platform environment that shows cyclicity and rhythmicity in facies architectures.

Acknowledgements The authors would like to thank Total for funding Olivier Dubrule professorship at Imperial College and the Department of Earth Science and Engineering at Imperial College for a scholarship to Thomas Le Blevec.

References

Alabert F (1989) Non-gaussian data expansion in the earth sciences. Terra Nova 1(2):123–134

Amour F, Mutti M, Christ N, Immenhauser A, Agar SM, Benson GS, Tomás S, Alway R, Kabiri L (2012) Capturing and modelling metre-scale spatial facies heterogeneity in a jurassic ramp setting (central high atlas, morocco). Sedimentology 59(4):1158–1189

Armstrong M, Galli A, Beucher H, Loc'h G, Renard D, Doligez B, Eschard R, Geffroy F (2011) Plurigaussian simulations in geosciences. Springer Science & Business Media

Astrakova A, Oliver DS, Lantuéjoul C (2015) Truncation map estimation based on bivariate probabilities and validation for the truncated plurigaussian model. arXiv preprint arXiv:150801090

Beucher H, Renard D (2016) Truncated gaussian and derived methods. Comptes Rendus Geoscience 348(7):510–519

Burgess P, Wright V, Emery D (2001) Numerical forward modelling of peritidal carbonate parasequence development: implications for outcrop interpretation. Basin Research 13(1):1–16

Burgess PM (2016) Identifying ordered strata: Evidence, methods, and meaning. Journal of Sedimentary Research 86(3):148–167

Carle SF, Fogg GE (1996) Transition probability-based indicator geostatistics. Mathematical geology 28(4):453–476

Chiles JP, Delfiner P (2012) Geostatistics: modeling spatial uncertainty, vol 497. John Wiley & Sons

Deutsch C, Tran T (2002) Fluvsim: a program for object-based stochastic modeling of fluvial depositional systems. Computers & Geosciences 28(4):525–535

Deutsch JL, Deutsch CV (2014) A multidimensional scaling approach to enforce reproduction of transition probabilities in truncated plurigaussian simulation. Stochastic environmental research and risk assessment 28(3):707–716

Doligez B, Hamon Y, Barbier M, Nader F, Lerat O, Beucher H, et al (2011) Advanced workflows for joint modelling of sedimentological facies and diagenetic properties. impact on reservoir quality. In: SPE Annual Technical Conference and Exhibition, Society of Petroleum Engineers

Doveton JH (1994) Theory and applications of vertical variability measures from Markov Chain analysis. AAPG Special Volumes

Dubrule O (2017) Indicator variogram models: Do we have much choice? Mathematical Geosciences pp 1–25

Egenhoff SO, Peterhänsel A, Bechstädt T, Zühlke R, Grötsch J (1999) Facies architecture of an isolated carbonate platform: tracing the cycles of the latemar (middle triassic, northern italy). Sedimentology 46(5):893–912

Emery X, Lantuéjoul C (2006) Tbsim: A computer program for conditional simulation of three-dimensional gaussian random fields via the turning bands method. Computers & Geosciences 32(10):1615–1628

Emery X, Arroyo D, Peláez M (2014) Simulating large gaussian random vectors subject to inequality constraints by gibbs sampling. Mathematical Geosciences 46(3):265–283

Freulon X, de Fouquet C (1993) Conditioning a gaussian model with inequalities. In: Geostatistics Troia92, Springer, pp 201–212

Galli A, Le Loch G, Geffroy F, Eschard R (2006) An application of the truncated pluri-gaussian method for modeling geology. AAPG Special Volumes

Genz A (1992) Numerical computation of multivariate normal probabilities. Journal of computational and graphical statistics 1(2):141–149

Goldhammer R, Dunn P, Hardie L (1990) Depositional cycles, composite sea-level changes, cycle stacking patterns, and the hierarchy of stratigraphic forcing: examples from alpine triassic platform carbonates. Geological Society of America Bulletin 102(5):535–562

Goldhammer R, Lehmann P, Dunn P (1993) The origin of high-frequency platform carbonate cycles and third-order sequences (lower ordovician el paso gp, west texas): constraints from outcrop data and stratigraphic modeling. Journal of Sedimentary Research 63(3)

Hinnov LA, Goldhammer RK (1991) Spectral analysis of the middle triassic latemar limestone. Journal of Sedimentary Research 61(7)

Hönig MR, John CM (2015) Sedimentological and isotopic heterogeneities within a jurassic carbonate ramp (uae) and implications for reservoirs in the middle east. Marine and Petroleum Geology 68:240–257

Jacquemyn C, Huysmans M, Hunt D, Casini G, Swennen R (2015) Multi-scale three-dimensional distribution of fracture-and igneous intrusion-controlled hydrothermal dolomite from digital outcrop model, latemar platform, dolomites, northern italy. AAPG Bulletin 99(5):957–984

Johnson NM, Dreiss SJ (1989) Hydrostratigraphic interpretation using indicator geostatistics. Water Resources Research 25(12):2501–2510

Jones TA, Ma YZ (2001) Teacher's aide: geologic characteristics of hole-effect variograms calculated from lithology-indicator variables. Mathematical Geology 33(5):615–629

Journel A, Froidevaux R (1982) Anisotropic hole-effect modeling. Mathematical Geology 14(3):217–239

Langlais V, Beucher H, Renard D (2008) In the shade of the truncated gaussian simulation. In: Proceedings of the eighth international geostatistics congress, pp 799–808

Lantuéjoul C (1994) Non conditional simulation of stationary isotropic multigaussian random functions. In: Geostatistical Simulations, Springer, pp 147–177

Lantuéjoul C (2013) Geostatistical simulation: models and algorithms. Springer Science & Business Media

Le Blévec T, Dubrule O, John CM, Hampson GJ, et al (2016) Building more realistic 3-d facies indicator models. In: International Petroleum Technology Conference

Le Blévec T, Dubrule O, John CM, Hampson GJ (2017) Modelling asymmetrical facies successions using pluri-gaussian simulations. In: Geostatistics

Valencia 2016, Springer, pp 59–75
Li W (2007) Markov chain random fields for estimation of categorical variables. Mathematical Geology 39(3):321–335
Lindsay RF, Cantrell DL, Hughes GW, Keith TH, Mueller III HW, Russell SD (2006) Ghawar Arab-D reservoir: widespread porosity in shoaling-upward carbonate cycles, Saudi Arabia. AAPG Special Volumes
Ma YZ, Jones TA (2001) Teacher's aide: Modeling hole-effect variograms of lithology-indicator variables. Mathematical Geology 33(5):631–648
Ma YZ, Seto A, Gomez E (2009) Depositional facies analysis and modeling of the judy creek reef complex of the upper devonian swan hills, alberta, canada. AAPG bulletin 93(9):1235–1256
Maleki M, Emery X, Cáceres A, Ribeiro D, Cunha E (2016) Quantifying the uncertainty in the spatial layout of rock type domains in an iron ore deposit. Computational Geosciences 20(5):1013–1028
Matheron G (1968) Processus de renouvellement purs. Course document Ecole des Mines de Paris
Matheron G, Beucher H, de Fouquet C, Galli A, Ravenne C (1988) Simulation conditionnelle à trois faciès dans une falaise de la formation du brent. Sciences de la Terre, Série Informatique Géologique 28:213–249
Middleton GV (1973) Johannes walther's law of the correlation of facies. Geological Society of America Bulletin 84(3):979–988
Obermaier M, Ritzmann N, Aigner T (2015) Multi-level stratigraphic heterogeneities in a triassic shoal grainstone, oman mountains, sultanate of oman: Layer-cake or shingles? GeoArabia 20(2):115–142
Parks KP, Bentley LR, Crowe AS (2000) Capturing geological realism in stochastic simulations of rock systems with markov statistics and simulated annealing. Journal of Sedimentary Research 70(4):803–813
Peterhänsel A, Egenhoff SO (2008) Lateral variabilities of cycle stacking patterns in the latemar, triassic, italian dolomites. SEPM Spec Publ 89:217–229
Pratt BR, James NP (1986) The st george group (lower ordovician) of western newfoundland: tidal flat island model for carbonate sedimentation in shallow epeiric seas. Sedimentology 33(3):313–343
Preto N, Hinnov LA, Hardie LA, De Zanche V (2001) Middle triassic orbital signature recorded in the shallow-marine latemar carbonate buildup (dolomites, italy). Geology 29(12):1123–1126
Purkis S, Vlaswinkel B, Gracias N (2012) Vertical-to-lateral transitions among cretaceous carbonate faciesa means to 3-d framework construction via markov analysis. Journal of Sedimentary Research 82(4):232–243
Pyrcz MJ, Deutsch CV (2014) Geostatistical reservoir modeling. Oxford university press
Read J, Goldhammer R (1988) Use of fischer plots to define third-order sea-level curves in ordovician peritidal cyclic carbonates, appalachians. Geology 16(10):895–899
Renard D, Beucher H (2012) 3d representations of a uranium roll-front deposit. Applied Earth Science 121(2):84–88

Sena CM, John CM (2013) Impact of dynamic sedimentation on facies heterogeneities in lower cretaceous peritidal deposits of central east oman. Sedimentology 60(5):1156–1183

Shinozuka M (1971) Simulation of multivariate and multidimensional random processes. The Journal of the Acoustical Society of America 49(1B):357–368

Strasser A (1988) Shallowing-upward sequences in purbeckian peritidal carbonates (lowermost cretaceous, swiss and french jura mountains). Sedimentology 35(3):369–383

Wackernagel H (2013) Multivariate geostatistics: an introduction with applications. Springer Science & Business Media

Wilkinson BH, Drummond CN, Rothman ED, Diedrich NW (1997) Stratal order in peritidal carbonate sequences. Journal of Sedimentary research 67(6)